Charge-Transport Properties of F_6TNAP-based Charge-Transfer Cocrystals

Raghunath R. Dasari,[a] Xu Wang,[b] Ren A. Wiscons,[c] Hamna F. Haneef,[d] Ajith Ashokan,[a] Yadong Zhang,[a] Marina S. Fonari,[b] Stephen Barlow,[a] Veaceslav Coropceanu,[a] Tatiana V. Timofeeva,[b] Oana D. Jurchescu,[c] Jean-Luc Brédas,[a] Adam J. Matzger,[c] Seth R. Marder*[a]

Dr. R. R. Dasari, A. Ashokan,[+] Dr. Y. Zhang, Dr. S. Barlow, Dr. V. Coropceanu, Prof. J.-L Brédas, Prof. S. R. Marder

School of Chemistry and Biochemistry and Center for Organic Photonics and Electronics (COPE)

Georgia Institute of Technology

Atlanta, GA, 30332 USA
E-mail: seth.marder@chemistry.gatech.edu

X. Wang,[+] Dr. M. S. Fonari, Prof. T. V. Timofeeva

Department of Biology and Chemistry,

New Mexico Highlands University,

Las Vegas, NM, 87701 USA

R. A. Wiscons,[+] Prof. A. J. Matzger

Department of Chemistry and the Macromolecular Science & Engineering Program,

The University of Michigan, Ann Arbor, MI 48109 USA

This is the author manuscript accepted for publication and has undergone full peer review but has not been through the copyediting, typesetting, pagination and proofreading process, which may lead to differences between this version and the Version of Record. Please cite this article as doi: 10.1002/adfm.201904858.

H. F. Haneef,[+] Prof. O. D. Jurchescu

Department of Physics and Center for Functional Materials,

Wake Forest University, Winston Salem, NC, 27019, USA

Dr. M. S. Fonari

Institute of Applied Physics, Chisinau MD-2028, Moldova

[+]These authors made equal contributions.

Keywords: Donor-acceptor cocrystals, crystal packing, electronic couplings, charge transport, mobility values

Abstract:

The crystal structures of the charge-transfer (CT) cocrystals formed by the π-electron acceptor 1,3,4,5,7,8-hexafluoro-11,11,12,12-tetracyanonaphtho-2,6-quinodimethane (F_6TNAP) with the planar π-electron-donor molecules triphenylene (TP), benzo[*b*]benzo[4,5]thieno[2,3-*d*]thiophene (BTBT), benzo[1,2-*b*:4,5-*b'*]dithiophene (BDT), pyrene (PY), anthracene (ANT), and carbazole (CBZ) have been determined using single-crystal X-ray diffraction, along with those of two polymorphs of F_6TNAP. All six cocrystals exhibit 1:1 donor / acceptor stoichiometry and adopt mixed-stacking motifs. Cocrystals based on BTBT and CBZ π-electron donor molecules exhibit brickwork packing, while the other four CT cocrystals show herringbone-type crystal packing. Infrared spectroscopy, molecular geometries determined by single-crystal X-ray diffraction, and electronic structure calculations indicate that the extent of ground-state charge transfer in each cocrystal is small. Density functional theory calculations predict large conduction bandwidths and, consequently, low effective masses for electrons for all six CT cocrystals, while the TP-, BDT-, and PY-based cocrystals are also predicted to have large valence bandwidths and low effective masses for holes. Charge-carrier mobility values were obtained from space-charge limited current (SCLC) measurements and field-effect transistor measurements, with values exceeding 1 $cm^2\ V^{-1}\ s^{-1}$ being estimated from SCLC measurements for BTBT:F_6TNAP and CBZ:F_6TNAP cocrystals.

1. Introduction

Cocrystals consist of a regular arrangement of two or more neutral molecular species in a defined stoichiometry and can exhibit properties distinct from those of their individual components. In charge-transfer (CT) cocrystals, one component acts as an π-electron donor (D) and another component acts as a π-electron acceptor (A), and both are typically planar molecules in order to facilitate CT interactions in the solid state. Two major types of molecular stacking motifs are found in CT crystals with 1:1 stoichiometry: mixed stacks, in which D and A molecules alternate along the stacking direction, -D-A-D-A, and segregated stacks, in which donor and acceptor molecules form separate stacks, -D-D-D- and -A-A-A.[1-3]

When free of disorder, metallic conductivities can be obtained along the stacking direction of CT cocrystals that form segregated stacks and that exhibit extents of CT approximately midway (ρ = ca. 0.5) between the completely neutral (ρ = 0) and fully ionic (ρ = 1) limits.[1-4] On the other hand, CT cocrystals that consist of mixed stacks generally behave as semiconductors or insulators.[3,5] Recently there has been increasing interest in the semiconducting[6-18] and photoconductive[19-21] properties of mixed-stack cocrystals. Large charge-carrier mobility values, μ, have been reported for several examples using space-charge limited current (SCLC) or field-effect transistor (FET) measurements, including coronene:TCNQ (μ_{SCLC} = 0.3 $cm^2\ V^{-1}\ s^{-1}$)[12] and DBTTF:TCNQ (DBTTF = dibenzotetrathia fulvalene; TCNQ = 7,7,8,8-tetracyanoquinodimethane) ($\mu_{e,FET}$ = 1.0 $cm^2\ V^{-1}\ s^{-1}$).[13] Notably, density functional theory (DFT) calculations have predicted that several mixed-stack CT crystals based on TCNQ and its 2,3,5,6-tetrafluoro analog (F_4TCNQ) acceptors possess small hole *and* electron effective masses along the stacking directions, suggesting ambipolar charge-transport properties.[10] Indeed, ambipolar transport has been found for field-effect transistors of some CT materials, such as single crystals of DBTTF:TCNQ, in which subtle effects of the solid-state packing lead to dominant electron-transport in the α-polymorph, and hole-dominant charge transport in the β-polymorph.[18]

While F_4TCNQ has often been used as an acceptor in CT cocrystals,[17, 22-27] its naphthalene analog, 1,3,4,5,7,8-hexafluoro-11,11,12,12-tetracyano-2,6-naphthoquinodimethane (F_6TNAP, also known as F_6TCNNQ), has been less well-studied. As a result of its extended π-system, F_6TNAP has a slightly more anodic reduction potential[28] and higher electron-affinity than F_4TCNQ.[29] Until very recently, reports on F_6TNAP (Figure 1) were limited to demonstrating its use as a *p*-dopant (*i.e.*, as a 1-electron oxidant) for organic hole-transport materials;[28-31] however, its properties also suggest it to be an excellent candidate for formation of CT cocrystals. Indeed, although p-doping ideally occurs through electron-transfer from the hole-transport material to the dopant, in the case of planar semiconductor and dopant molecules, CT complexes can be obtained instead with concomitantly less efficient generation of charge carriers;[32] for example, CT complex formation has been observed when F_6TNAP is used to *p*-dope diindeno[1,2,3-*cd*:1',2',3'-*lm*]perylene or 2,2':5',2'':5'',2''':5''',2'''':5'''',2'''''-sexithiophene, although the single-crystal structures of the CT complexes were not determined.[33] In 2018, Kloc and co-workers reported crystal structures for mixed-stack cocrystals of F_6TNAP with four planar donor molecules – triphenylene, pyrene, phenanthrene, and naphtho[1,2-*b*:5,6-*b'*]dithiophene – along with estimates of the extent of CT based on vibrational spectroscopy.[34]

Here we disuss the electronic band structure and electrical properties of donor:acceptor cocrystals based on F_6TNAP. We consider cocrystals with six different donors, two of which – triphenylene (TP) and pyrene (PY) – were also used in Kloc's study, while the others – benzo[*b*]benzo[4,5]thieno[2,3-*d*]thiophene (BTBT), benzo[1,2-*b*:4,5-*b'*]dithiophene (BDT), anthracene (ANT), and carbazole (CBZ) – were chosen based on their oxidation potentials (shown in Figure 1 along with DFT-derived HOMO energies; similar variations are seen in values of DFT ionization energies, Table S1),[35] which are similar those of the first two and indicating that the donor-to-F_6TNAP electron-transfer reactions in solution would all be endergonic by ca. 0.5-0.8 eV

The structures of these cocrystals, along with those of two polymorphs of the neat acceptor,

F_6TNAP, were determined by single-crystal X-ray diffraction (SCXRD), enabling their electronic structure to be studied using DFT calculations. Charge-transport properties were investigated by field-effect transistor (FET) and space-charge-limited current (SCLC) measurements, and the results were correlated with the predictions obtained from band-structure calculations.

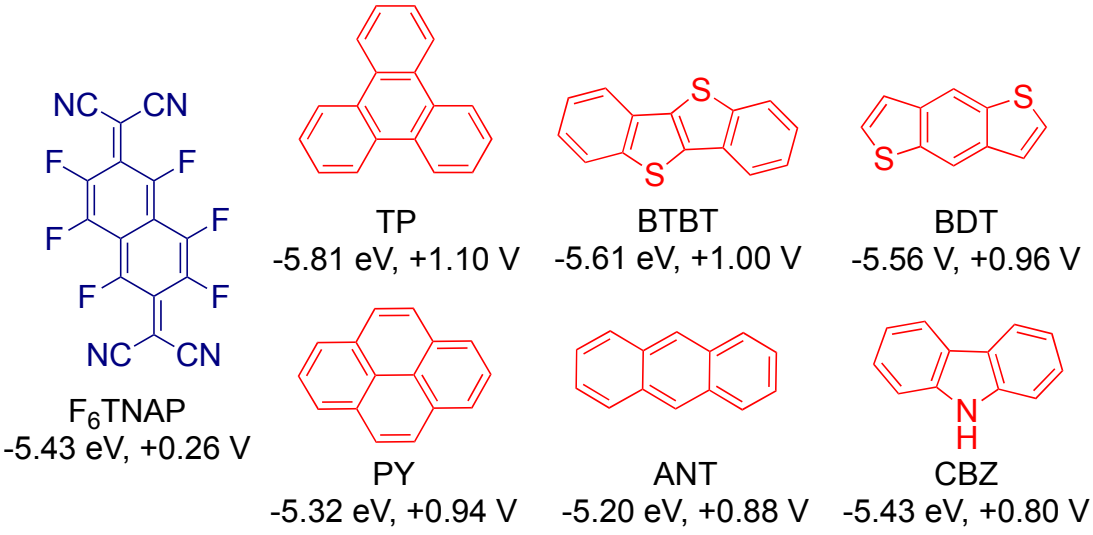

Figure 1. Molecular structures for F_6TNAP, triphenylene (TP), benzo[*b*]benzo[4,5]thieno[2,3-*d*]thiophene (BTBT), benzo[1,2-*b*:4,5-*b'*]dithiophene (BDT), pyrene (PY), anthracene (ANT), and carbazole (CBZ) and along with calculated (B3LYP/6-31G) LUMO and HOMO energies (eV) for the acceptor and the donors, respectively, and solution electrochemical reduction and oxidation potentials (V vs. $FeCp_2^{+/0}$; see Table S1 for more details) for the acceptor and the donors, respectively.

2. Results and Discussion

2.1. Crystal Structures of F_6TNAP

F_6TNAP (synthesized following the reported procedure[36]) was found to crystallize – both upon solvent evaporation and physical vapor deposition – as a physical mixture of two crystal forms, consistent with previous reports.[36] These two forms can be differentiated by luster, color, and habit; form I crystallizes as green blocks with a metallic luster and form II as red-orange plates without a metallic appearance. SCXRD indicates that these two crystal forms represent two polymorphs of F_6TNAP. Form I crystallizes in the $R\bar{3}$ space group with a half F_6TNAP molecule in the asymmetric unit located on an inversion center. In addition, the naphthalene portion of the F_6TNAP molecule is disordered over two positions (Figure S1). Close F…F and CN…CF contacts formed between three adjacent F_6TNAP molecules (see Figure 2a) give rise to the three-fold symmetry axis parallel to the *c*-axis characteristic of form I (see Figure 2b). Form II crystallizes in the $P2_1/c$ space group and also contains half of a F_6TNAP molecule in the asymmetric unit; however, unlike form I, it is free of the positional disorder. While molecules of F_6TNAP interact exclusively through edge-to-face π-π interactions in form I, form II shows both edge-to-face (see Figure 2c) and slipped face-to-face π-π interactions producing a herringbone motif (see Figure 2d).

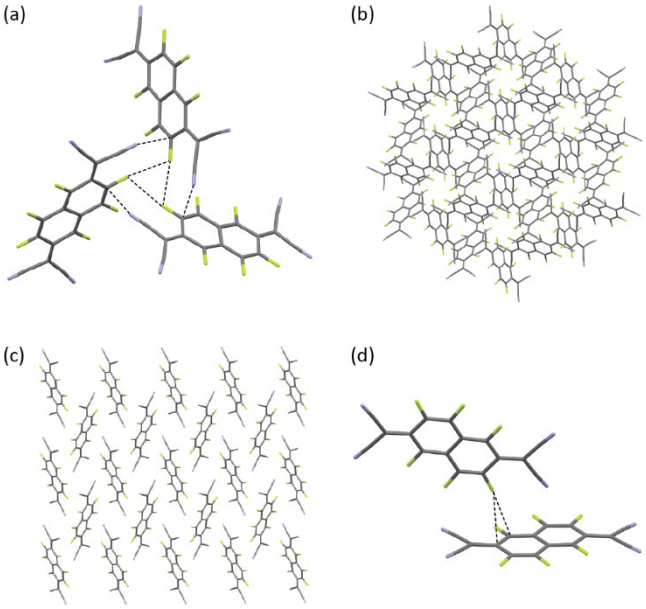

Figure. 2. (a) F...F and CN...CF close contacts (shown as dashed black lines) formed between adjacent F_6TNAP molecules in form I; (b) view down the *c*-axis of F_6TNAP form I, highlighting the 3-fold symmetry (disorder is omitted for clarity); (c) view down the *a*-axis of F_6TNAP form II, highlighting the herringbone motif; (d) edge-to-face interactions between F_6TNAP molecules in form II.

2.2. Cocrystal preparation and structure

All six cocrystals were crystallized by evaporation from dichloromethane solutions, but this method did not produce single crystals of CBZ:F_6TNAP suitable for SCXRD structure determination. Single crystals of CBZ:F_6TNAP were produced instead by slow interdiffusion of a dichloromethane solution of the donor and an acetonitrile solution of the acceptor. All cocrystals showed prismatic or needle-like morphologies and were more deeply and differently colored than either of the pure components, suggesting electronic interaction between the donor and acceptor molecules in the cocrystal phases.

The structures of the six CT cocrystals were elucidated by SCXRD, confirming that all of the cocrystals form in a 1:1 donor / acceptor stoichiometry and adopt a mixed-stacking motif. In each case donors and acceptors are almost parallel, with significant overlap of their π-faces (Figure 3), and

π-stacking interaction distances that fall within the range of 3.25(2) – 3.39(2) Å (Table 1), substantially shorter than the sum of the van der Waals radii for two carbon atoms (3.5 Å) and consistent with strong D-A interactions. The relationship between different stacks results in brickwork-like packing in the structures of BTBT:F_6TNAP and CBZ:F_6TNAP, and herringbone-like packing in the other four structures, as shown in Figure 4. Further information regarding the packing, including the interstack interactions, is given in the supporting information (Figures S1-S3; Tables S2-S4).

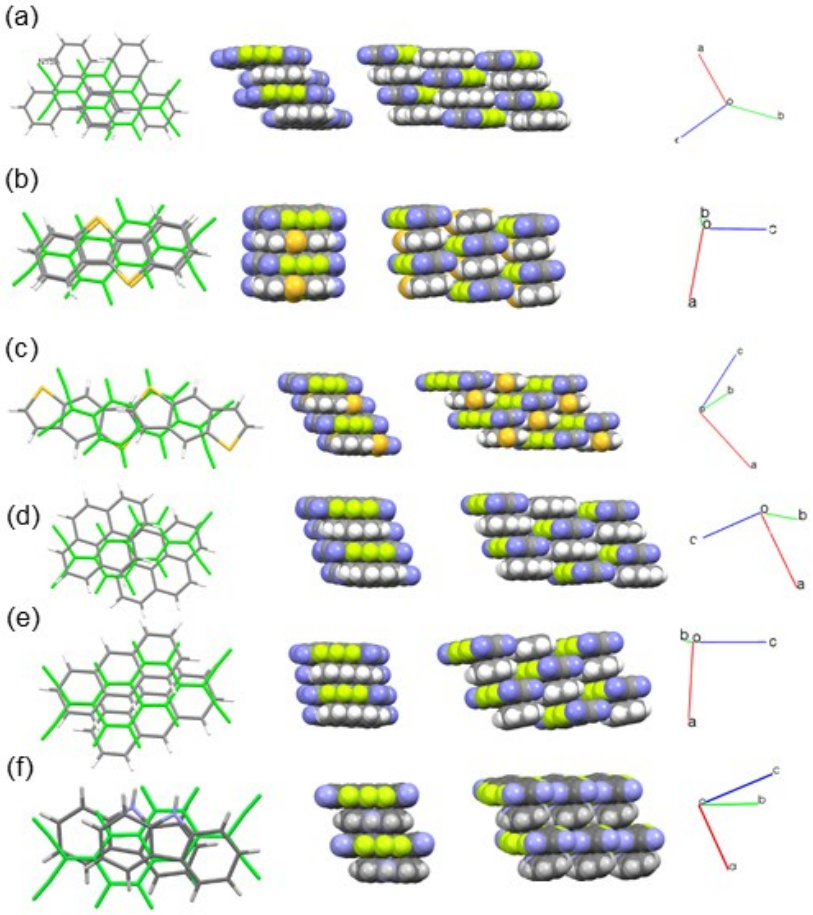

Figure 3. Overlapping D-A patterns in projection on the F_6TNAP (marked in green) mean plane and space-filling presentation (side and front) of stacks in (a) TP:F_6TNAP (for one crystallographically unique D-A pair); (b) BTBT:F_6TNAP; (c) BDT:F_6TNAP; (d) PY:F_6TNAP; (e) ANT:F_6TNAP; and (f). CBZ:F_6TNAP.

Table 1. D-A interplanar angles and the shortest D-A distances (Å) in the TP:F_6TNAP, BTBT:F_6TNAP, BDT:F_6TNAP, ANT:F_6TNAP, CBZ:F_6TNAP, and PY:F_6TNAP complexes.

Compound	D-A angle / °	D-A distance[a] / Å
TP:F_6TNAP[b]	2.40	3.28-3.39
	1.26	3.24-3.39
BTBT:F_6TNAP	1.17	3.35-3.39
BDT:F_6TNAP	0.94	3.34-3.38
PY:F_6TNAP	1.79	3.25-3.34
ANT:F_6TNAP	4.51	3.33-3.36
CBZ:F6TNAP	3.59	3.36-3.37

[a] D-A distances were calculated as the shortest distances from the atom in the donor moiety to the average plane of the F_6TNAP acceptor. [b] The two sets of values refer to two crystallographically independent stacks in the structure.

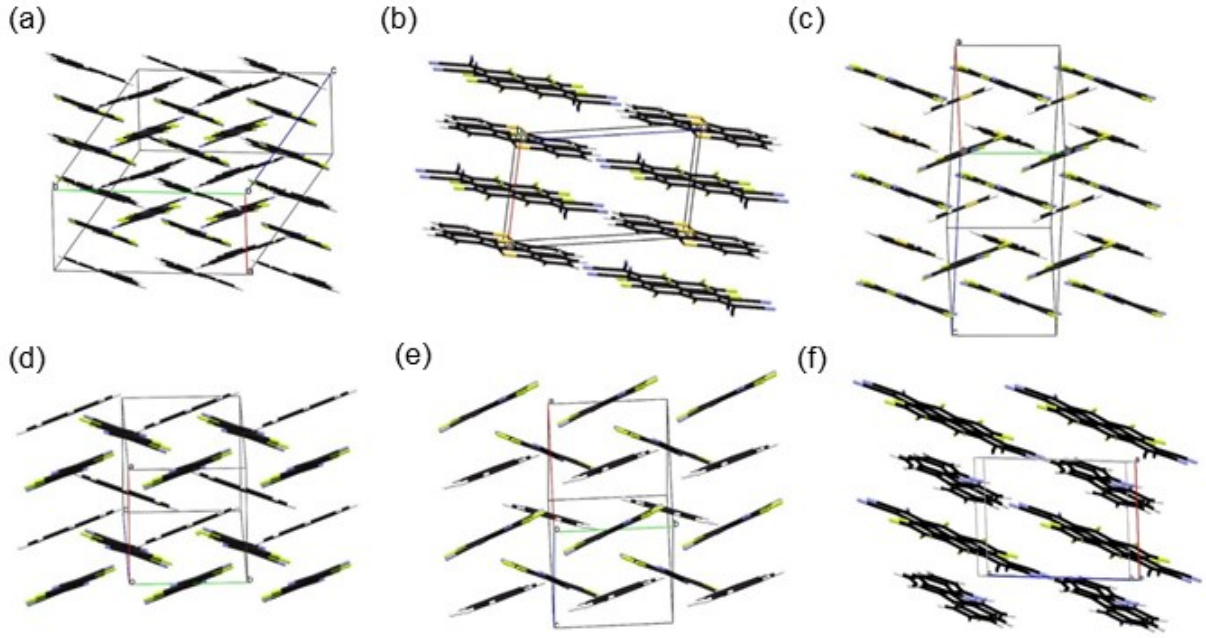

Figure 4. Crystal packing of the (a) TP:F_6TNAP, (b) BTBT:F_6TNAP, (c) BDT:F_6TNAP, (d) PY:F_6TNAP, (e) ANT:F_6TNAP and (f) CBZ:F_6TNAP single crystals.

The structure of TP:F_6TNAP obtained in the present work is essentially identical to that previously reported.[34] Our structure of PY:F_6TNAP differs from the reported structure in the extent of disorder (90:10 vs. 50:50 occupancy of two different acceptor positions), as well as exhibiting small differences in cell parameters and molecular orientation; these differences are presumably attributable to the different crystal-growth methods used in the two studies (solution evaporation vs. vapor-phase transport).

2.3. Degree of Charge Transfer

An important parameter in CT cocrystals such as these is the degree of CT, ρ, between D and A; here ρ = 0 corresponds to completely neutral molecules with no significant intermolecular π-overlap, a value of ρ = 1 indicates a salt consisting of non-interacting radical ions, while good intrastack charge transport in both segregated- and mixed-stack structures is associated with intermediate values, *i.e.*, partial CT.[3] The molecular geometries of the donor molecules in the present cocrystals are generally similar to those in the crystal structures of the neutral donor compounds,[37-43] while the F_6TNAP moieties in the cocrystal structures generally exhibit quinoidal patterns of bond-length alternation similar (Table S3) to those in the structures of the two F_6TNAP polymorphs[42] (Figure S4), together suggesting a low value of ρ.[44]

The nitrile stretching frequencies of cyano-functionalized acceptors such as F_6TNAP have been found to be sensitive to the charge on the acceptor molecules,[31] and several previous studies of cocrystals of acceptors including TCNQ,[45,46] F_4TCNQ,[16, 47-48] F_6TNAP,[34] and 2,3-dihalo-5,6-dicyanobenzoquinones,[49] have used these frequencies to obtain values of ρ. That said, the sensitivity of these stretching frequencies to a variety of local interactions,[50] as well as the acceptor charge, means that derived values of ρ should only be regarded as approximate. In addition, electron-phonon effects can also complicate the interpretation of vibrational spectra. [51-53] The IR spectrum of neutral F_6TNAP (Form I) exhibit three peaks attributable to nitrile stretches at 2225 cm^{-1}

(weak), 2214 cm^{-1} (strong), and 2204 cm^{-1} (weak), consistent with previous reports.[34] IR spectra were measured for the cocrystals and, consistent with previous studies, the frequency of the highest energy mode was used to estimate values of ρ for each cocrystal according to:

$$\rho = \frac{2\Delta\nu}{\nu_0\left(1-\nu_1^2/\nu_0^2\right)} \quad (1)$$

where $\Delta\nu = \nu_0 - \nu_{CT}$ and ν_0, ν_1, and ν_{CT} denote the highest nitrile stretching frequencies of F_6TNAP in the neutral state (ρ = 0, ν_0 = 2225 cm^{-1}), the F_6TNAP anion (ρ = 1, ν_1 = 2194 cm^{-1}),[31] and the CT cocrystal, respectively. In the case of CBZ:F_6TNAP, the value of ν_{CT} was experimentally indistinguishable from that of ν_0, likely the outcome of the competing effects of CT and CN...HN hydrogen bonding (i.e., a particularly severe effect of the local environment) on the stretching frequency (see Figure S5), precluding its use in estimating ρ; hydrogen bonding may also be responsible for the differences between this cocrystal and the other five in the pattern of relative intensities for the nitrile stretching modes (see Figure S5). For the other five cocrystals, small values of ρ (Table S5) – ranging from 0.06±0.03 to 0.13±0.03 – were obtained, consistent with the neutral-like patterns of bond length seen in the crystal structures, and with the endergonicity of electron transfer suggested by the similar redox potentials of donors (see Figure 1). Values for TP:F_6TNAP (0.06±0.03) and PY:F_6TNAP (0.13±0.03) are similar to those previously reported[34] when the substantial experimental uncertainties (which arise due to the small values of ρ and, therefore, $\Delta\nu$) are taken into account.

2.4. Electronic Structure

To characterize the electronic structure of the six cocrystals, density functional theory (DFT) calculations were performed at the B3LYP/6-31G level. The derived band structures and the density of states are shown in Figure 5. Table 2 compares the widths of the conduction band (CB) and valence band (VB), along with the effective masses, for each cocrystal (see also Table S6 and Figure

S6 for more details regarding effective masses and transfer integrals, respectively). The largest CB bandwidth of about 480 meV is estimated for BTBT:F_6TNAP (Figure 5b), which is somewhat larger than the largest value (445 meV) computed at the same level of theory for cocrystals based on F_4TCNQ.[21] The largest band dispersion is found along the stacking direction and is due to a large effective (super-exchange) transfer integral (76 meV) along this direction (see Figure S6). A relatively large CB bandwidth (320 meV) is also found for CBZ:F_6TNAP. The VBs are significantly narrower than the CBs for BTBT:F_6TNAP, ANT:F_6TNAP, and CBZ:F_6TNAP. For BDT:F_6TNAP the VB approaches the CB in width, while for TP:F_6TNAP and PY:F_6TNAP the VB is somewhat wider than the CB. Thus, the present systems do not exhibit the usual "mirror" symmetry between VBs and CBs found in many previously studied cocrystals.[54,55] The lack of the mirror symmetry is an indication that the super-exchange coupling is not dominated by the interaction involving only the donor and acceptor molecular frontier orbitals (a situation found in many CT systems) but rather contains contributions from more molecular levels. As a result, the super-exchange transfer integrals, t^{eff}, for holes can be very different than for electrons; in the present systems for which these couplings are overall smaller for holes than for electrons (see Figure S6 and Table S6).[54] We also note that the superexchange couplings depend on the transfer integrals (t_{DA}) between donor and acceptor frontier orbitals and the related energy gaps (E_{DA}); thus in the weak electronic coupling limit they are given by:[10]

$$t^{eff} = t_{DA}^2/\Delta E_{DA} \qquad (2)$$

The DFT results show that despite 0.5 eV variation in the E_{DA} values the t_{DA} integrals, which are controlled by the crystal packing, have a stronger effect on the relative superexchange couplings among considered systems (see Table S6).

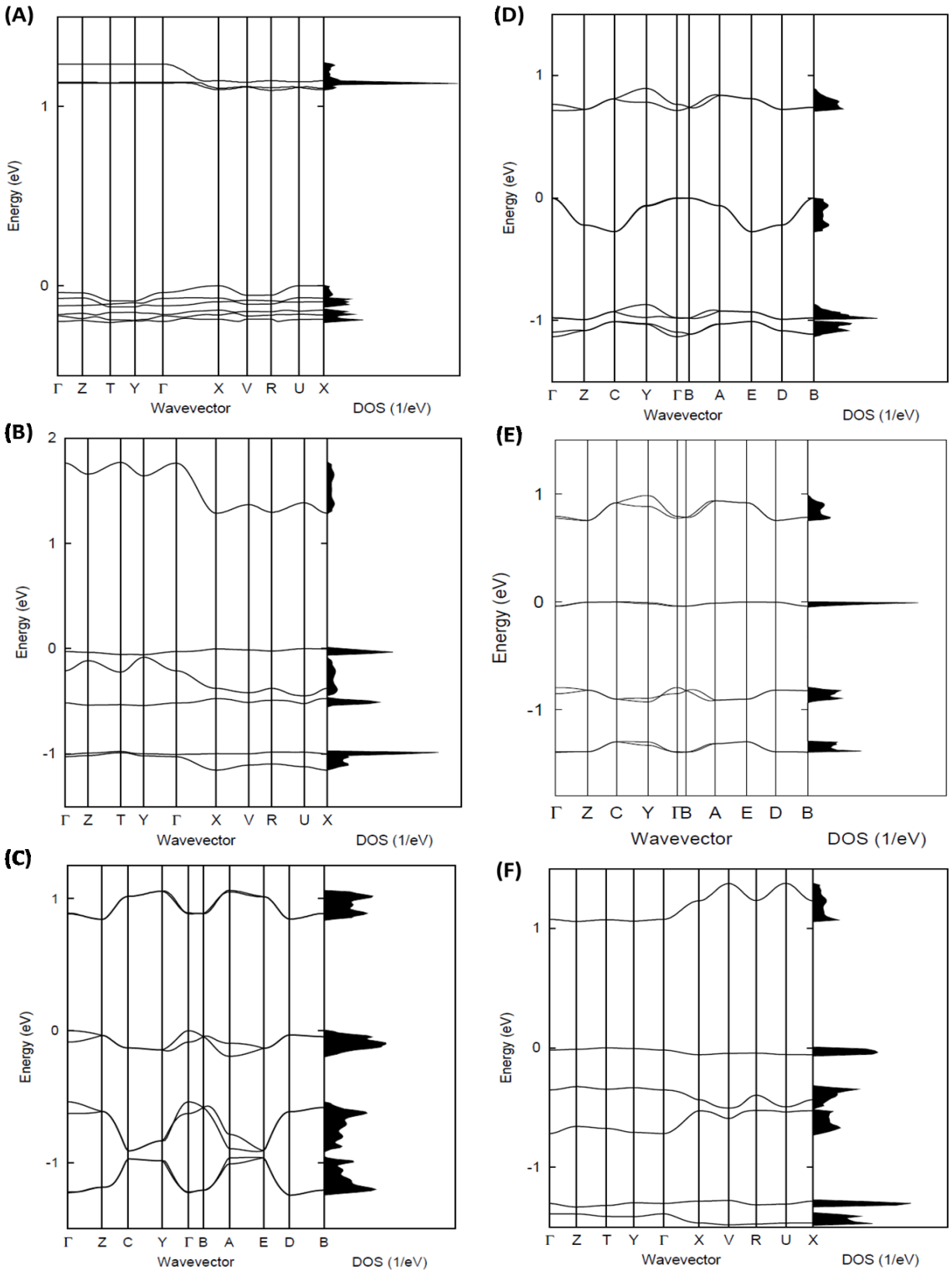

Figure 5. Electronic band structure and density of states of (A) TP:F_6TNAP, (B) BTBT:F_6TNAP, (C) BDT:F_6TNAP, (D) PY:F_6TNAP, (E) ANT:F_6TNAP, and (F) CBZ:F_6TNAP crystals. The special points in the first Brillouin zone are labelled as: Γ = (0,0,0), Z = (0,0,0.5), T = (0,0.5,0.5), Y = (0,0.5,0), X = (0.5,0,0), V = (0.5,0.5,0), R = (0.5,0.5,0.5) and U = (0.5,0,0.5), for (A, B & F) cases, and Γ = (0,0,0), Z = (0,0.5,0), C = (0.5,0.5,0), Y = (0.5,0,0), B = (0,0,0.5), A = (-0.5,0,0.5), E = (-0.5,0.5,0.5) and D = (0,0.5,0.5) for (C, D & E) cases. All points are given in fractional coordinates of the reciprocal space. The zero of energy is taken as the top of valence band.

Table 2. B3LYP/6-31G conduction and valence bandwidths (in meV) along with the lowest two effective masses (in units of electron mass in vacuum, m_0).

Cocrystal	Valence Bandwidth	Conduction Bandwidth	Effective Mass, Holes		Effective Mass, Electrons	
			m_1 / m_0	m_2 / m_0	m_1 / m_0	m_2 / m_0
TP:F_6TNAP	220	156	1.2	>10	1.4	2.7
BTBT:F_6TNAP	57.4	482	4.5	>10	0.6	1.4
BDT:F_6TNAP	194	212	1.0	3.1	0.8	>10
PY:F_6TNAP	272	181	1.2	5.0	2.8	>10
ANT:F_6TNAP	37.2	231	>10	>10	1.8	>10
CBZ:F_6TNAP	57.6	318	4.5	>10	0.7	7.6

In line with the results for the band dispersion and transfer integrals, the smallest effective masses for electrons are found along the stacking direction. Except in the case of PY:F_6TNAP, the effective mass for electrons are smaller than $2m_0$, where m_0 is the electron mass in vacuum. In particular very small effective mass values of 0.64 m_0 and 0.75 m_0 are found for BTBT:F_6TNAP and CBZ:F_6TNAP, respectively. Small effective masses of 1.25 m_0, 1.00 m_0, and 1.25 m_0 are also found for holes in TP:F_6TNAP, BDT:F_6TNAP, and PY:F_6TNAP, respectively. However, in contrast to what is found for electrons, the smallest effective masses for holes are found along the stacking direction only in BDT:F_6TNAP, while in TP:F_6TNAP and PY:F_6TNAP cocrystals, they are found along directions approximately perpendicular to the stacking direction (see Table S7), which is a consequence of the direct through-space transfer integrals in these systems exceeding the super-exchange couplings. In the most cases the charge carriers are characterized with a small effective mass only along one crystal direction. However, two small components of the effective masses are found for the

electrons in TP:F_6TNAP and BTBT:F_6TNAP and for holes in BDT:F_6TNAP, suggesting that the charge transport in these cases has a two-dimensional character. For comparison, we note that the calculated effective masses for holes and electrons in pentacene, which is one of the most extensively studied single-component systems in organic electronics, are ca. 1.5 m_0 and 1.6 m_0, respectively.[56]

Overall, the calculations predict good electron-transport properties in all six cocrystals, particularly for BTBT:F_6TNAP and CBZ:F_6TNAP cocrystals, whereas good hole-transport properties are also predicted for TP:F_6TNAP, BDT:F_6TNAP, and PY:F_6TNAP, suggesting that these three cocrystals could display ambipolar transport.

2.5. Electrical Properties

Two-terminal current-voltage characteristics were measured for all six cocrystal types (see Figure S7 for sample geometry) and the charge-carrier mobility values, μ, were evaluated first by using the space-charge-limited current (SCLC) method. The SCLC model was initially developed for vacuum tubes and later adopted by Mott and Gurney to describe single-carrier injection in a trap-free insulator,[57] modified by Rose and Lampert for an insulator with localized trapping states in the gap,[58,59] and first used to characterize transport in organic crystals by Helfrich and Mark in 1962.[60] Since then, the SCLC method has adopted for the study of charge transport in both crystalline and amorphous organic semiconductors, although its use is challenged by the numerous approximations that are necessary to obtain charge-carrier mobilities.[61-64]

In our crystals, based on evaluation of crystal shapes using experimental data with diffractometer goniometer and simulated crystal morphology (Figure S8), it is expected that charge transport probed in these measurements is along the molecular π-stacking axes. Figure 6 shows current-voltage characteristics for BTBT:F_6TNAP and CBZ:F_6TNAP as representative examples, while data for the other cocrystals are shown in Figure S9. The resistivity, ρ, was calculated from the low-voltage regime of the curve, in which the current density *J* versus the applied voltage *V* follows an

ohmic relation ($J \propto V$, indicated by the blue line). Charge-carrier mobility values, μ, were estimated from the SCLC regime, in which the current density has a quadratic dependence on the applied voltage ($J \propto V^2$), by using the Mott-Gurney law:

$$J_{\mathrm{SCLC}} = \frac{9}{8}\frac{\mu\varepsilon_{\mathrm{r}}\varepsilon_0\theta}{L^3}V^2 \qquad (3)$$

where L is the distance between the contacts, ε_{r} is the relative permittivity of the semiconductor (approximated to be 3), ε_0 is the permittivity of free space, and θ the ratio of free charge carriers to total charge carriers (assumed to be 1).[65] Note that the Mott-Gurney law ignores diffusion currents and assumes unipolar transport and a single discrete distribution of shallow traps. When the energy of trapping states is distributed over a wider energetic range, as is the case in many crystals, more complicated *J*-*V* relations may be obtained, e.g., $J \propto V^n$ with $n > 2$.[66] In the present case, mobility values were estimated from the region of the double logarithmic *J*-*V* plot with a slope of ca. 2, indicated with a red line in Figure 6. The slopes of the two regions used to determine the resistivity and mobility are 1.3 and 2.3, respectively, for BTBT:F_6TNAP, and 1.1 and 2.0, respectively, for CBZ:F_6TNAP; the close correspondence between these values and the ideal values of 1 and 2 for Ohmic and SCLC regimes, respectively, supports the use of this model.

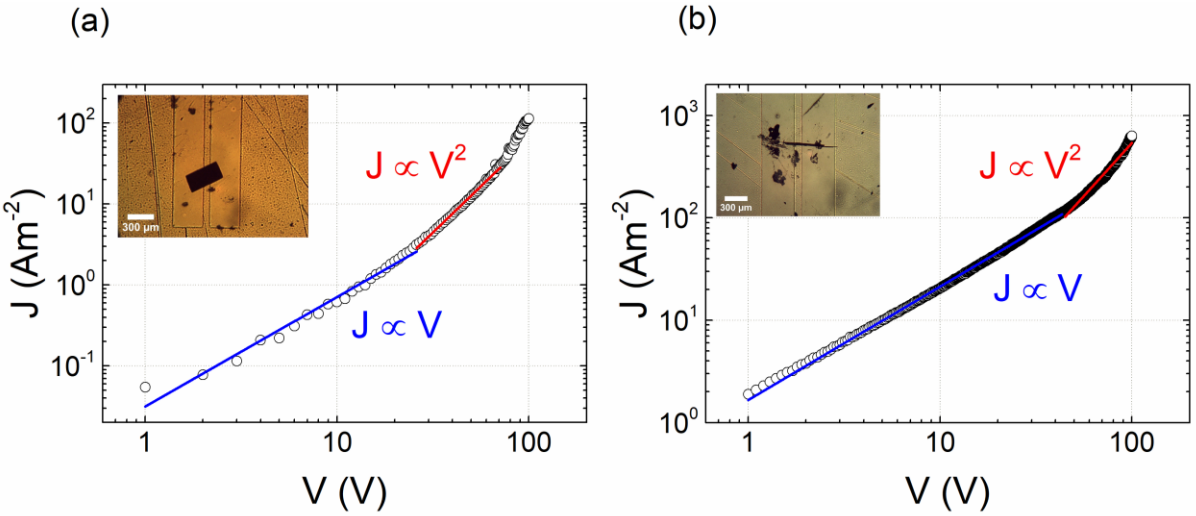

Figure 6. SCLC measurements for the (a) BTBT:F_6TNAP, and (b) CBZ:F_6TNAP co-crystals. Inset shows an optical micrograph of a crystal laminated across the electrodes. The blue and red solid lines represent linear fits for the ohmic and SCLC regimes, respectively.

Table 3 lists the values of μ obtained for all six cocrystals. Since there are significant uncertainties in the estimation of μ values from SCLC measurements that arise with the assumed values of θ and ε_r and with measurements of crystal thickness, we report the order of magnitude, rather than actual values. More details on the calculations can be found in Section IV of the Supplementary Information. We considered $\vartheta = 1$, which is the upper limit for this parameter and corresponds to a trap-free regime. In these measurements, it is likely that that the trap-free region has not been reached and, thus, that a value $\theta < 1$ should be used. Thus, assuming, $\vartheta = 1$ leads to underestimation of μ. On the other hand, if ε_r or crystal thickness are larger, μ is overestimated. Nevertheless, it is clear that the mobilities fall into two groups: TP:F_6TNAP, BTBT:F_6TNAP, PY:F_6TNAP, and CBZ:F_6TNAP exhibit charge transport properties comparable with the best obtained in charge transfer complexes, with mobilities in the 0.1 – 1 $cm^2\ V^{-1}\ s^{-1}$ range, while the mobilities are substantially lower for BDT:F_6TNAP and ANT:F_6TNAP. Overall, in this series, BTBT:F_6TNAP and CBZ:F_6TNAP cocrystals, which both exhibit brickwork-like crystal packing and for which the conduction bandwidths are largest of any of the bandwidths calculated in this work, show estimated SCLC mobility values exceeding 1 $cm^2\ V^{-1}\ s^{-1}$.

Table 3. Summary of electrical properties evaluated from SCLC and OFET measurements.

Cocrystal	SCLC Measurements[a]	OFET Characteristics	
	μ_{SCLC} / $cm^2 V^{-1} s^{-1}$	μ_h / $cm^2 V^{-1} s^{-1}$	μ_e / $cm^2 V^{-1} s^{-1}$
TP:F_6TNAP	10^{-1}	-	-
BTBT:F_6TNAP	10^{0}	-	-
BDT:F_6TNAP	10^{-4}	-	-
PY:F_6TNAP	10^{-1}	$(1.4 \pm 0.42) \times 10^{-2}$	$(2.0 \pm 0.71) \times 10^{-2}$
ANT:F_6TNAP	10^{-3}	$(3.8 \pm 0.14) \times 10^{-4}$	$(6.6 \pm 0.49) \times 10^{-4}$
CBZ:F_6TNAP	10^{1}	-	-

[a]Reported as an order of magnitude because these values are estimated with numerous approximations. See section IV, Table S8, in the supporting information for more details.

Evaluation of cocrystal electrical properties was also attempted using bottom-gate bottom-contact organic field-effect transistors (OFETs) (Figure S7). ANT:F_6TNAP and PY:F_6TNAP crystals yielded functional FETs (see Figures 7 and S10, respectively, for transfer characteristics), while for the other systems, our attempts to fabricate OFETs were unsuccessful, most likely due to the high surface roughness of these crystals. We minimized the scaterring processes at the semiconductor/dielectric interface by employing a structure with air-gap dielectric, as described in detail in the Exmerimental section. This interface is free of polaronic effects and strain,[67-68] but it is not exempt from the trapping resulting from imperfections at the crystal surface. Crystal step edges present on the surfaces of organic semiconductors single crystal were found to be trapping sites for the charges accumulated at the interface betwen the crystal and the dielectric.[69] While we do not have a quantitalive analysis of the density of the step edges in our crystals, by simple optical inspection it can be clearly seen that their density is very high.

Figure 7 shows the current between the source and drain electrodes, I_D, as a function of gate-source voltage (V_{GS}) at constant source-drain voltage, V_{DS} = –60 V (left panel) and V_{DS} = +60 V (right panel) for an ANT:F_6TNAP device, which clearly indicate ambipolar transport. The electron and

hole charge carrier mobilities were evaluated in the respective saturation regimes using standard OFET equations,[70-73] and are given in Table 3. Ambipolar charge transport has been observed in other charge-transfer complexes, with the magnitude being determined by the nature of contacts used for source and drain electrdes, and the details of the molecular packing.[74-75] The *IV*-curves for PY:F_6TNAP devices are included in Figure S10, and the electron and hole mobilities are listed in Table 3. The reliability factors for each of these devices are included in the figure caption.

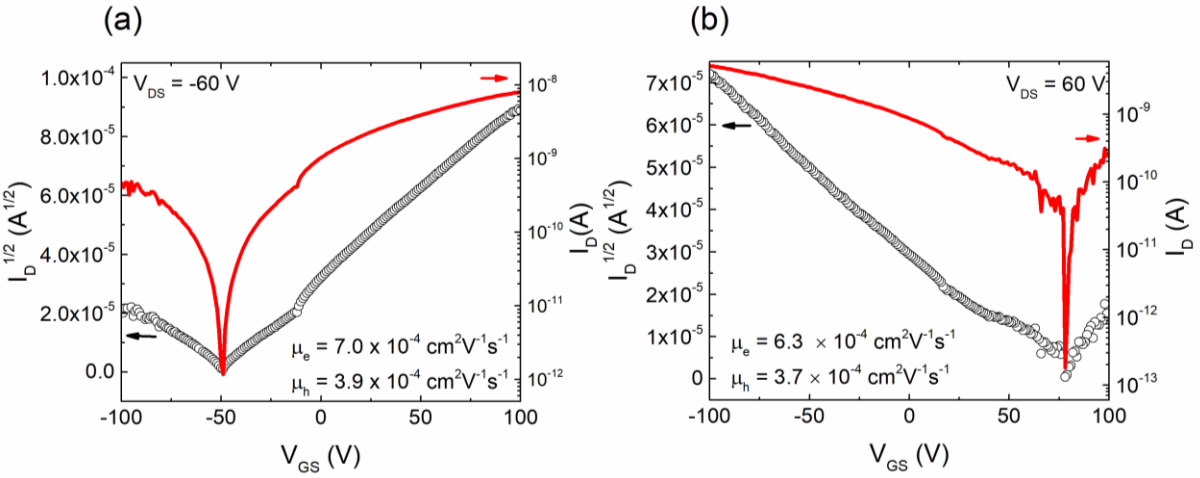

Figure 7. Evolution of the drain current, I_D as a function of gate-source voltage, V_{GS} for (a) ANT:F_6TNAP at V_{DS} = –60 V, and (b) V_{DS} = 60 V. The left axis shows the square root of I_D while the right axis shows I_D on a logarithmic scale. The reliability factor for the graph in panel (a) is 87%, and for the graph in panel (b) 94%.

The charge-carrier mobility values determined from SCLC measurements (μ_{SCLC}) are about one order of magnitude higher than those determined from FET measurements (μ_{FET}) for ANT:F_6TNAP and PY:F_6TNAP devices. This discrepancy may arise for several reasons. First, μ_{SCLC} values are representative of the bulk of the crystal, while μ_{FET} values reflect electrical properties at the surface, where interactions at the surface/dielectric interface, such as surface roughness (see Figure S11) cause charge scattering, typically leading to less efficient transport. Second, the Mott-Gurney

model assumes unipolar charge injection, while the FET results clearly indicate that these crystals exhibit ambipolar transport. When both electrons and holes coexist in the crystal, charge recombination and neutralization occur, resulting in an increase in the net charge density, which leads to an enhancement of the current and overestimation of SCLC mobilities.

The ambipolarity observed for the PY:F_6TNAP cocrystal is broadly consistent with the band-structure calculations, which indicate large widths for both VB and CB. On the other hand, the calculated VB bandwidth for the ANT cocrystal is much lower than the CB bandwidth, apparently at odds with the ambipolarity suggested by the FET mobility data; this might be due to preferential trapping of electrons at the dielectric interface reducing electron mobility. The estimated relatively high μ_{SCLC} values for CBZ:F_6TNAP and BTBT:F_6TNAP are consistent with calculated large CB bandwidths and low effective masses; however, trends in μ_{SCLC} values for other cocrystals show no obvious correlation with the trends in calculated bandwidths or effective masses. For example, similar bandwidths and effective masses are obtained for PY:F_6TNAP and BDT:F_6TNAP, yet the μ_{SCLC} value estimated for the latter is over three orders of magnitudes than for the former. This may reflect large variations in trap densities and / or in surface effects that impair carrier injection between different crystals.[76] Electron-phonon coupling[77] and disorder, neither of which are accounted for in the present calculations, may also play a role in the discrepancies between experimental and theoretical trends in transport properties.

3. Conclusions

Six 1:1 cocrystals of F_6TNAP with planar donors have been characterized by X-ray diffraction, IR spectroscopy, DFT calculations, and electrical measurements. All six crystals contain mixed donor / acceptor stacks with significant overlap of donor and acceptor π-faces. The molecular geometries seen in the crystal structures, as well as the nitrile stretching frequencies seen in infra-red spectra, indicate a small degree of donor-to-acceptor charge transfer in each of these cocrystals, consistent

with the redox potentials of the donors and acceptor, which indicate that donor-to-acceptor electron transfer in solution would be endergonic by ca. 0.5-0.8 eV.

DFT calculations afford large conduction bandwidths and low effective masses for electrons along the stacking direction for all six cocrystals, suggesting good electron transport. Large valence bandwidths and low effective hole masses are also found for three of the crystals (TP:F_6TNAP, BDT:F_6TNAP, and PY:F_6TNAP), albeit only along the stacking direction in the case of the BDT cocrystal, suggesting ambipolar transport properties. Four of the cocrystals exhibit charge-carrier mobilities in excess of 10^{-1} cm^2 V^{-1} s^{-1}, similar to the highest values reported in other charge-transfer compunds. Field-effect transistors demonstrate balanced ambipolar behavior with hole- and electron-transport mobilities being lower than the value determined from SCLC measurements.

Overall our results indicate that F_6TNAP is a promising building block for use, along with planar donor molecules, in obtaining crystals with good charge-transport properties. Future work should concentrate on selecting additional partner donors of comparable size and with appropriate ionization energies, allowing for formation of mixed-stacks with considerable D:A π-orbital overlap.

4. Experimental Section

General Synthesis and Characterization: F_6TNAP was synthesized following the reported procedure;[36] donor molecules were obtained from commercial sources. Electrochemical measurements were carried out under nitrogen in dry deoxygenated 0.1 M tetra-n-butylammonium hexafluorophosphate in dry dichloromethane using a CH Instruments CHI620D Electrochemical Workstation CHI620D and a conventional three-electrode cell with a glassy carbon working electrode, platinum wire counter electrode, and an Ag wire coated with AgCl as the pseudo-reference electrode. Potentials were referenced to ferrocenium/ferrocene by using internal ferrocene. Cyclic voltammograms were recorded at a scan rate of 50 mV s^{-1}. Infrared spectra were

measured on Shimadzu IRPrestige-21 Fourier Transform Infrared Spectrophotometer or a Thermo Nicolet Avatar 360 FT-IR instrument in ATR mode using a germanium window (SpectraTech). The sample chamber was purged with N_2 to minimize background from atmospheric absorption. The reflectance was scanned over a range of 800-3800 cm^{-1}. The spectra were collected and the default Ge ATR correction applied in EZ OMNIC 2.11 (Thermo Fisher Scientific) and analyzed in ACD/Spectrus Processor 2014.

F_6TNAP Polymorph Preparation: Crystals of the two polymorphs were grown by sublimation in a gradient tube furnace under flow of N_2 gas (5 mL/min) using 0.25 inch standard-wall glass tubes. The temperature was set to 265.0(2) °C and maintained for 3 h. The two forms can also be prepared by evaporation of solutions of F_6TNAP in dry acetonitrile or dichloromethane on polypropylene and glass substrates.

Cocrystal Preparation: For most of the cocrystals, a dichloromethane solution (1 mL) of the donor (0.0165 mmol) was added to a dichloromethane solution (40 mL) of F_6TNAP acceptor (0.0165 mmol). The solution was kept in a narrow glass tube and solvent was allowed to evaporate. The resulting crystals were vacuum filtered to obtain needle-like solids. CBZ:F_6TNAP crystals were obtained by separately dissolving F_6TNAP (0.02 mmol) in N_2-sparged acetonitrile (0.5 mL) and carbazole (0.02 mmol) in N_2-sparged dichloromethane (0.5 mL); the acetonitrile solution was layered over the dichloromethane solution and crystals allowed to grow by solvent diffusion at 0 °C.

Single Crystal X-ray Diffraction: Single-crystal X-ray diffraction data for the two polymorphs of F_6TNAP and for CBZ:F_6TNAP were collected using a Rigaku XtaLAB Synergy-S X-ray diffractometer configured in a kappa goniometer geometry. The diffractometer is equipped with a low temperature device and a PhotonJet-S microfocus Cu source (λ = 1.54187 Å) set at a rough divergence of 9.5 and operated at 50 kV and 1 mA. X-ray intensities were measured at 298(3) K with the HyPix-6000HE detector placed 34.00 mm from the sample. The data were processed with CrysAlisPro v38.46 (Rigaku Oxford Diffraction) and corrected for absorption. The structures were solved in OLEX2[78] using SHELXS[79] and refined using SHELXL.[80] All non-hydrogen atoms were refined anisotropically.

The single-crystal X-ray diffraction data for the other five cocrystals, TP:F_6TNAP, BTBT:F_6TNAP, BDT:F_6TNAP, ANT:F_6TNAP, and PY:F_6TNAP were collected a the Bruker SMART APEX II diffractometer with CCD area detector (graphite monochromated MoKα radiation, λ = 0.71073 Å, ω-scans with a 0.5° step in ω) at 100 K. Absorption corrections were applied using the semi empirical method of the SADABS program for all samples reported. [81] All the frames were integrated with the Bruker SAINT software package using a narrow frame algorithm. The structures were solved and refined using the Bruker SHELXTL Software package.[80,82] Further details of the crystals and their structural refinements are given in Table S2 and, in cif format in CCDC 1922856-1922863.

No disorder was found in structure ANT:F_6TNAP; in four other crystal structures the components reveal different disordering patterns (Figure S2): in TP:F_6TNAP one of two crystallographically unique F_6TNAP molecules is inverted to show two orientations with different occupancies, 0.7304(19) and 0.2696(19); in PY:F_6TNAP the F_6TNAP molecule is disordered with occupancies 0.9019(17) and 0.0981(17); in BDT-F_6TNAP both F_6TNAP (with occupancies 0.8569(17) and 0.1431(17)) and BDT (equal occupancies) are disordered; while in BTBT:F_6TNAP only the BTBT molecule is inverted (two orientations with the occupancies 0.9424(9) and 0.0576(9)).

Computational Methodology: Individual molecular energy levels were calculated using the Density Functional Theory (DFT) at B3LYP/6-31G level of theory. Since an earlier investigation found no major difference between the optimized and experimental crystal structures in the calculation of electronic properties,[54] experimental geometries were used for the calculation of band structure and density of states for these systems, which were also calculated at B3LYP/6-31G level of theory. Uniform 8×4×4, 10×8×6, 8×8×4, 8×8×4, 8×10×4, and 8×8×8 Monkhorst-Pack k-point mesh was employed for the TP:F_6TNAP, BTBT:F_6TNAP, BDT:F_6TNAP, PY:F_6TNAP, ANT:F_6TNAP, and CBZ:F_6TNAP crystals, respectively. All band structure calculations were performed using CRYSTAL 14 package.[83,84]

The inverse effective mass tensor for the 3-dimensional crystal is calculated using

$$\frac{1}{m_{ij}} = \frac{1}{\hbar^2}\left(\frac{d^2E}{dk_j dk_i}\right) \quad (4)$$

where, subscripts *i* and *j* represent the Cartesian coordinates in reciprocal space. $\hbar$ is the Planck constant, and *k* is the electron wave-vector. Diagonalization of m_{ij}^{-1} provides the principal components and their orientations. The inverse effective mass tensor was calculated by means of Sperling's centered difference method with $dk = 0.01$ bohr^{-1}.

The electronic coupling (transfer integral) between different components is an important metric for the evaluation of wave-function overlap between different units. In a crystal, the extent of charge delocalization between subsequent units can be quantified using this metric. In this work, the effective transfer integrals between neighboring molecules along different directions were calculated by using a molecular-fragment orbital approach combined with basis-set orthogonalization procedure at the B3LYP/6-31G level of theory. The electronic coupling along the stacking direction (super-exchange coupling), t_{eff}, are estimated with an energy-splitting approach by considering the orbital energies, *E*, of a A-D-A triad,[21]

$$t_{eff} = \frac{(E_{L+1} - E_L)}{2} \quad (5)$$

or D-A-D triad,

$$t_{eff} = \frac{(E_H - E_{H-1})}{2} \quad (6)$$

where the subscripts L and L+1 refer to the LUMO and LUMO+1 of the neutral state of the A-D-A triad, and H and H–1 to the HOMO and HOMO–1 of the D-A-D triad. The calculations of the transfer integrals (electronic coupling) were performed using the Gaussian 09 D01 package.[85]

Device Fabrication and Electrical Measurements: Organic field-effect transistors (OFETs, Figure S7) were obtained by laminating the single crystals over pre-fabricated elastomeric polydimethylsiloxane (PDMS) stamps.[86-88] In this structure, a 5.5 µm thick gap between the raised and recessed regions of the PDMS stamp served as the air/vacuum gate dielectric. A layer of 40 nm of Au was e-beam evaporated on the patterned PDMS stamp to form electrically isolated electrodes with the source and drain defined on the raised region and the gate on the recessed region of the PDMS stamp. Space-charge-limited current (SCLC) measurements were performed in the same configuration, with the coplanar contacts using non-gated two-point current-voltage measurements. Both OFET and SCLC measurements were performed at room temperature, in the dark and under vacuum using an Agilent 4155C Semiconductor Parameter Analyzer. At least 5 crystals of each type were measured, in each case giving consistent results. SCLC measurements were taken in incremental voltage steps of 0.1 V and FET measurements were performed in 1 V steps. Background noise was minimized by integrating the measurements over longer times, during which the instrument averages several measurement samples. The medium integration time was used in all measurements; this is automatically adjusted by the instrument depending on the current level: smaller current requires longer the integration time (50 PLC needed for a current of 10 pA, 5 PLC for 1 nA, and 1 PLC for 10 nA to 100 mA, where PLC is the power-line cycle mode and 1 PLC=1/60 s).

[CCDC 1922856-1922863 contains the supplementary crystallographic data for this paper. These data can be obtained free of charge from The Cambridge Crystallographic Data Centre via www.ccdc.cam.ac.uk/data_request/cif.]

Acknowledgements

This material is based upon work supported by the U. S. Army Research Laboratory and the U. S. Army Research Office under contract/grant number W911NF-13-1-0387, and by the National Science Foundation under grant DMR-1627925, DMR-1708147, and DMR-1523611 (PREM program). We thank Cameron H. Feriante for acquiring the AFM data shown in Figure S11.

Received: ((will be filled in by the editorial staff))
Revised: ((will be filled in by the editorial staff))
Published online: ((will be filled in by the editorial staff))

References

[1] T. Mori, T. Kawamoto, *Annu. Rep. Prog. Chem., Sect. C: Phys. Chem*. **2007**, *103*, 134.

[2] T. Hasegawa, J. Takeya, *Sci. Technol. Adv. Mater.* **2009**, *10*, 024314.

[3] K. P. Goetz, D. Vermeulen, M. E. Payne, C. Kloc, L. E. McNeil, O. D. Jurchescu, *J. Mater. Chem. C*, **2014**, *2*, 3065.

[4] J. Ferraris, D. O. Cowan, V. Walatka, Jr., J. H. Perlstein, *J. Am. Chem. Soc*. **1973**, *95*, 948.

[5] Metallic-type temperature-dependent conductivity has also been reported for one CT cocrystal example: G. Saito, S.-S. Pac, O. O. Drozdova, *Synth. Met.* **2001**, *120*, 667.

[6] S. K. Park, S. Varghese, J. H. Kim, S.-J. Yoon, O. K. Kwon, B.-K. An, J. Gierschner, S. Y. Park, *J. Am. Chem. Soc.* **2013**, *135*, 4757.

[7] A. A. Sagade, K. V. Rao, S. J. George, A. Datta, G. U. Kulakarni, *Chem. Commun.* **2013**, *49*, 5847.

[8] W. Zhu, Y. Yi, Y. Zhen, W. Hu, *Small*, **2015**, *11*, 2150.

[9] Y. Qin, J. Zhang, X. Zheng, H. Geng, G. Zhao, W. Xu, W. Hu, Z. Shuai, D. Zhu. *Adv. Mater.* **2014**, *26*, 4093.

[10] L. Zhu, Y. Yi, Y, Li, E.-G. Kim, V. Coropceanu**,** J.-L. Brédas, *J. Am. Chem. Soc.* **2012**, *134*, 2340.

[11] A. A. Mandal, P. Swain, B. Nath, S. Sau, P. Mal, *CrystEngComm*, **2019**, *21*, 981.

[12] X. Chi, C. Besnard, V. K. Thorsmølle, V. Y. Butko, A. J. Taylor, T. Siegrist, A. P. Ramirez, *Chem. Mater*. **2004**, *16*, 575.

[13] Y. Takahashi, T. Hasegawa, Y. Abe, Y. Tokura, K. Nishimura, G. Saito. *Appl. Phys. Lett.*, **2005**, *86*, 063504.

[14] K. Ijima, R. Sanada, D. Yoo, R. Sato, T. Kawamoto, T. Mori *ACS Appl. Mater. Interf.* **2018**, *10*, 10262.

[15] Y. Takahashi, T. Hasegawa, Y. Abe, Y. Tokura, G. Saito. *Appl. Phys. Lett.* **2006**, *88*, 073504.

[16] J. Zhang, H. Geng, T. S. Virk, Y. Zhao, J. Tan, C. a. Di, W. Xu, K. Singh, W. Hu, Z. Shuai, Y. Liu, D. Zhu, *Adv. Mater*. **2012**, *24*, 2603.

[17] K. P. Goetz, A. Fonari, D. Vermeulen, P. Hu, H. Jiang, P. J. Diemer, J. W. Ward, M. E. Payne, C. S. Day, C. Kloc, V. Coropceanu, L. E. McNeil, O. D. Jurchescu, *Nat. Commun.* **2014**, *5*, 5642.

[18] K. P. Goetz, J. y. Tsutsumi, S. Pookpanratana, J. Chen, N. S. Corbin, R. K. Behera, V. Coropceanu, C. A. Richter, C. A. Hacker, T. Hasegawa, O. D. Jurchescu, *Adv. Electron. Mater*. **2016**, *2*, 1600203.

[19] H.-D. Wu, F.-X. Wang, Y. Xiao, G.-B. Pan, *J. Mater. Chem. C*, **2014**, *2*, 2328.

[20] W. Yu, X.-Y. Wang, J. Li, Z.-T. Li, Y.-K. Yan, W. Wang, *Chem. Commun*. **2013**, *49*, 54.

[21] J. Tsutsumi, H. Matsui, T. Yamada, R. Kumai, T. Hasegawa, *J. Phys. Chem. C* **2012**, *116*, 23957.

[22] J. B. Torrance, J. J. Mayerle, K. Bechgaard, B. D. Silverman, Y. Tomkiewicz, *Phys. Rev. B,* **1980**, *22*, 4960.

[23] J. Zhang, W. Xu, P. Sheng, G. Zhao, D. Zhu, *Acc. Chem. Res*. **2017**, *50*, 1654.

[24] P. Hu, H. Li, Y. Li, H. Jiang, C. Kloc. *CrystEngComm*, **2017**, *19*, 618.

[25] R. Sato, M. Dogishi, T. Higashino, T. Kadoya, T. Kawamoto, T. Mori, *J. Phys. Chem. C,* **2017**, *121*, 6561.

[26] J. Zhang, G. Liu, Y. Zhou, G. Long, P. Gu, Q. Zhang, *ACS Appl. Mater. Interfaces* **2017**, *9*, 1183.

[27] T. J. Emge, W. A. Bryden, F. M. Wiygul, D. O. Cowan, T. J. Kistenmacher, *Chem. Phys*. **1982**, *77*, 3188.

[28] Y. Karpov, T. Erdmann, I. Raguzin, M. Al-Hussein, M. Binner, U. Lappan, M. Stamm, K. L. Gerasimov, T. Beryozkina, V. Bakulev, D. V. Anokhin, D. A. Ivanov, F. Günther, S. Gemming, G. Seifert, B. Voit, R. D. Pietro, A. Kiriy, *Adv. Mater.* **2016**, *28*, 6003.

[29] F. Zhang, A. Kahn, *Adv. Funct. Mater*. **2018**, *28*, 1703780.

[30] M. Thomschke, S. Reineke, B. Lüssem, K. Leo, *Nano Lett*. **2012**, *12*, 424.

[31] Y. Karpov, T. Erdmann, M. Stamm, U. Lappan, O. Gusakova, M. Malanin, I. Raguzin, T. Beryozkina, V. Bakulev, F. Günther, S. Gemming, G. Seifert, M. Hambsch, S. Mannsfeld, B. Voit, A. Kiriy, *Macromolecules*, **2017**, *50*, 914.

[32] I. Salzmann, G. Heimel, M. Oehzelt, S. Winkler, N. Koch, *Acc. Chem. Res*. **2016**, *49*, 370.

[33] G. Duva, L. Pithan, C. Zeiser, B. Reisz, J. Dieterle, B. Hofferberth, P. Beyer, L. Bogula, A. Opitz, S. Kowarik, A. Hinderhofer, A. Gerlach, F. Schreiber, *J. Phys. Chem.* **2018**, *122*, 18705.

[34] P. Hu, S. Wang, A. Chaturvedi, F. Wei, X. Zhu, X. Zhang, R. Li, Y. Li, H. Jiang, Y. Long, C. Kloc. *Cryst. Growth Des.* **2018**, *18*, 1776.

[35] With the exception of the computational data for ANT, the *trends* in these DFT values are also in generally good agreement with those in the electrochemical potentials.

[36] P. K. Koech, A. B. Padmaperuma, L. Wang, J. S. Swensen, E. Polikarpov, J. Darsell, J. E. Rainbolt, D. J. Gaspar, *Chem. Mater*. **2010**, *22*, 3926.

[37] M. Weck, A. R. Dunn, K. Matsumoto, G. W. Coates, E. B. Lobkovsky, R. H. Grubbs, *Angew. Chem. Int. Ed*. **1999**, *38*, 2741.

[38] X. Pang, H. Wang, W. Wang, W. J. Jin, *Cryst. Growth Des.* **2015**, *15*, 4938.

[39] C. P. Brock, J. D. Dunitz, *Acta Cryst*. **1990**. *B46*, 795.

[40] C. Niebel, Y. Kim, C. Ruzié, J. Karpinska, B. Chattopadhyay, G. Schweicher, A. Richard, V. Lemaur, Y. Olivier, J. Cornil, A. R. Kennedy, Y. Diao, W.-Y. Lee, S. Mannsfeld, Z. Bao. H. Geerts, *J. Mater. Chem. C*, **2015**, *3*, 674.

[41] C. Wang, H. Nakamura, H. Sugino, K. Takimiya, *J. Mater. Chem. C*, **2018**, *6*, 3604.

[42] In the structure of CBZ:F_6TNAP the bond length precision is relatively low, due to small crystal size and extensive disorder, and so the molecular geometries cannot be reliably described as either neutral or radical-ion like.

[43] The structure of BDT has not been reported, but those of closely related derivatives are reported in ref. [41] and their geometries are similar to those of the BDT moiety in the BDT:F_6TNAP structure.

[44] In principle, such a comparison of bond lengths can yield a quantitative estimate of ρ as done, for example, in the case of stilbene:F_4TCNQ.[16] However, this was not done in the present series due to the complicating effects of disorder in some of the structures (see Fig. S2) on the reliability of some of the bond lengths, and due to the relatively small extent of CT implied by IR measurements. However, it is clear from the X-ray data that the structures are much closer to the neutral limit than to the ionic.

[45] J. G. Robles-Martínez, A. Salmerón-Valverde, J. Argüelles-Ramírez, A. Zehe, *Mol. Eng*. **1999**, *8*, 411.

[46] A. Morherr, S. Witt, A. Chernenkaya, Jan-Peter Bäcker, G. Schönhense, M. Bolte, C. Krellner, *Physica B: Condensed Matter*, **2016**, *496*, 98.

[47] B. Mahns, O. Kataeva, D. Islamov, S. Hampel, F. Steckel, C. Hess, M. Knupfer, B. Büchner, C. Himcinschi, T. Hahn, R. Renger, *Cryst. Growth Des.* **2014**, *14*, 1338.

[48] P. Hu, K. Du, F. Wei, H. Jiang, C. Kloc, *Cryst. Growth Des*. **2016**, *16*, 3019.

[49] R. A. Wiscons, V. Coropceanu, A. J. Matzger, *Chem. Mater*. **2019**, published online, (doi: 10.1021/acs.chemmater.9b00502).

[50] M. Meneghetti, C. Pecile, *J. Chem. Phys*. **1986**, *84*, 4949.

[51] M. J. Rice, V. M. Yartsev, C. S. Jacobsen, C. Schelde, *Phys. Rev. B*, **1980**, *21*, 3437.

[52] A. Girlando, R. Bozio, C. Pecile, J. B. Torrance, *Phys. Rev. B*, **1982**, *26*, 2306.

[53] A. Painelli, A. Girlando, *J. Chem. Phys.* **1986**, *84*, 5655.

[54] L. Zhu, Y. Yi, A. Fonari, N. S. Corbin, V. Coropceanu, J.-L. Brédas, *J. Phys. Chem. C,* **2014**, *118*, 14150.

[55] R. K. Behera, N. R. Goud, A. J. Matzger, J.-L. Brédas, V. Coropceanu, *J. Phys. Chem. C,* **2017**, *121*, 23633.

[56] V. Coropceanu, Y. Li, Y. Yi, L. Zhu, J.-L. Brédas, *MRS Bulletin*, **2013**, *38*, 57.

[57] N. F. Mott, R. W. Gurney, *Electronic Processes in Ionic Crystals.* OxfordUniv. Press, Oxford: **1940**.

[58] A. Rose, *Phys. Rev.* **1955**, *97*, 1538.

[59] A. Rose, M. A. Lampert, *Phys. Rev.* **1959**, *113*, 1227.

[60] V. Helfrich, P. Z. Mark, *Physik.* **1962,** *166*, 370.

[61] V. Podzorov, S. E. Sysoev, E. Loginova, V. M. Pudalov, M. E. Gershenson, *Appl. Phys.Lett.* **2003**, *83*, 3504.

[62] O. D. Jurchescu, J. Baas, T. T. M. Palstra, *Appl. Phys.Lett.* **2004**, *84*, 3061.

[63] P. M. W. Blom, M. J. M. De Jong, J. J. M. Vleggaar, *Appl. Phys.Lett.* **1996**, *68*, 3308.

[64] J. Dacuna, A. Salleo, *Phys. Rev. B*, **2011**, *84*, 195209.

[65] K. P. Goetz, O. D. Jurchescu. *Handbook of Organic Materials for Electronic and Photonic Devices* (2nd Edition), Ed: O. Ostroverkhova, Woodhead Publishing, Elsevier, Amsterdam, Netherlands, **2019**, ISBN: 978-0-08-102284-9

[66] E. A. Silinsh, *Organic Molecular Crystals: Their electronic states,* Springer Berlin Heidelberg, Berlin, Heidelberg, **1980**.

[67] I. N. Hulea, S. Fratini, H. Xie, C. L. Mulder, N. N. Lossad, G. Rastelli, S. Ciuchi, A. F. Morpurgo, *Nat. Mater*. **2006**, *5*, 982.

[68] Y. Mei, P. J. Diemer, M. R. Niazi, R. K. Hallani, K. Jarolimek, C. S. Day, C. Risko, J. E. Anthony, A. Amassian, O. D. Jurchescu, *Proc. Natl. Acad. Sci*. **2017**, *114*, E6739.

[69] T. He, Y. Wu, G. D'Avino, E. Schmidt, M. Stolte, J. Cornil, D. Beljonne, P. P. Ruden, F. Würthner, C. D. Frisbie, *Nat.Commun*. **2018**, *9*, 2141.

[70] Z. A. Lamport, H. F. Haneef, S. Anand, M. Waldrip, O. D. Jurchescu, *J. Appl. Phys.*, **2018**, *124*, 071101.

[71] M. S. Kang, C. D. Frisbie, *ChemPhysChem*, **2013**, *14*, 1547.

[72] J. Zaumseil, H. Sirringhaus, *Chem. Rev*. **2007**, *107*, 1296.

[73] H. Klauk, *Chem. Soc. Rev*. **2010**, *39*, 2643.

[74] Y. Takahashi, *Appl. Phys. Lett*. **2006**, *88*, 073504.

[75] K. P. Goetz, J. Tsutsumi, S. Pookpanratana, J. Chen, N. S. Corbin, R. K. Behera, V. Coropceanu, C. A. Richter, C. A. Hacker, T. Hasegawa, O. D. Jurchescu. *Adv. Electron. Mater.* **2016**, *2*, 1600203.

[76] Some discrepancies may also be associated with temperature-dependent effects: electrical measurements were conducted at room temperature, whereas the crystal structures on which the calculations are based were mostly recorded at 100 K (with the exception of the CBZ cocrystal structure, which was determined at room temperature.

[77] A. M. Zeidell, L. Jennings, C. K. Frederickson, Q. Ai, J. J. Dressler, L. N. Zakharov, C. Risko, M. M. Haley, O. D. Jurchescu, *Chem. Mater.* **2019**, DOI: 10.1021/acs.chemmater.9b01436.

[78] O. V. Dolomanov, L. J. Bourhis, R. J. Gildea, J. A. K. Howard, H. Puschmann, *J. Appl. Cryst.* **2009**, *42*, 339.

[79] G. M. Sheldrick, *Acta Cryst. A* **2015**, *71*, 3.

[80] G. M. Sheldrick, *Acta Cryst. C* **2015**, *71*, 3.

[81] G. M. Sheldrick, Bruker/Siemens area detector absorption correction program, V.2.0.3; Bruker AXS: Madison, WI, 2003.

[82] G. M. Sheldrick, SHELXTL, v. 6.12 Structure Determination Software Suite; Bruker AXS: Madison, WI, 2001.

[83] R. Dovesi, R. Orlando, A. Erba, C. M. Zicovich-Wilson, B. Civalleri, S. Casassa, L. Maschio, M. Ferrabone, M. De La Pierre, P. D'Arco, Y. Noel, M. Causa, M. Rerat, B. Kirtman, Int. *J. Quantum Chem*. **2014**, *114*, 1287.

[84] R. Dovesi, V. R. Saunders, C. Roetti, R. Orlando, C. M. Zicovich-Wilson, F. Pascale, B. Civalleri, K. Doll, N. M. Harrison, I. J. Bush, P. D'Arco, M. Llunell, M. Causà and Y. Noël, CRYSTAL14 User's Manual (University of Torino, Torino, 2014).

[85] *Gaussian 09, Revision D.01*, **2009**, M. J. Frisch, G. W. Trucks, H. B. Schlegel, G. E. Scuseria, M. A. Robb, J. R. Cheeseman, G. Scalmani, V. Barone, B. Mennucci, G. A. Petersson, H. Nakatsuji, M. Caricato, X. Li, H. P. Hratchian, A. F. Izmaylov, J. Bloino, G. Zheng, J. L. Sonnenberg, M. Hada, M. Ehara, K. Toyota, R. Fukuda, J. Hasegawa, M. Ishida, T. Nakajima, Y. Honda, O. Kitao, H. Nakai, T. Vreven, J. A. Montgomery Jr., J. E. Peralta, F. Ogliaro, M. Bearpark, J. J. Heyd, E. Brothers, K. N. Kudin, V. N. Staroverov, R.Kobayashi, J. Normand, K. Raghavachari, A. Rendell, J. C. Burant, S. S. Iyengar, J. Tomasi, M. Cossi, N. Rega, J. M. Millam, M. Klene, J. E. Knox, J. B. Cross, V. Bakken, C. Adamo, J. Jaramillo, R. Gomperts, R. E. Stratmann, O. Yazyev, A. J. Austin, R. Cammi, C. Pomelli, J. W. Ochterski, R. L. Martin, K. Morokuma, V. G. Zakrzewski, G. A. Voth, P. Salvador, J. J. Dannenberg, S. Dapprich, A. D. Daniels, Ö. Farkas, J. B. Foresman, J. V. Ortiz, J. Cioslowski, and D. J. Fox, Gaussian, Inc., Wallingford CT.

[86] V. C. Sundar, J. Zaumseil, V. Podzorov, E. Menard, R. L. Willett, T. Someya, M. E. Gershenson, J. A. Rogers, *Science*, **2004**, *303*, 1644.

[87] E. Menard, V. Podzorov, S.-H. Hur, A. Gaur, M. E. Gershenson, J. A. Rogers, *Adv. Mater.* **2004**, *16*, 2097.

[88] M. J. Pereira, C. Ayela, L. Hirsch, I. Dufour, A. Briseno, M. Matta, Y. Olivier, L. Muccioli, A. Crosby, G. Wantz 19th International Conference on Solid-State Sensors, Actuators and Microsystems (TRANSDUCERS), IEEE, **2017**, 1163.

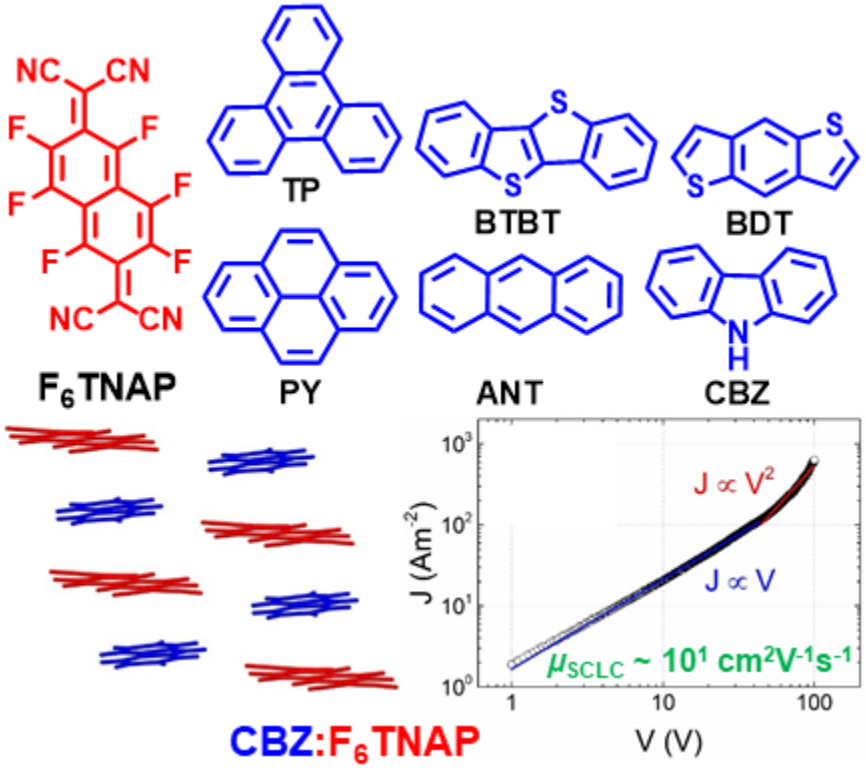

Structural, electronic band structure, and electrical properties of a series of charge-transfer cocrystals based on F_6TNAP acceptor, and six planar donors were presented. DFT calculations afford large conduction bandwidths and low effective masses for all six cocrystals. A couple of cocrystals exhibit charge-carrier mobilities in excess of 1 $cm^2\ V^{-1}\ s^{-1}$, as estimated from SCLC measurements.

Key word: Charge-transport